Research Article | Vol. 30, No. 9 / 25 Apr 2022 / Optics Express 15376
Optics EXPRESS

Standoff CARS spectroscopy and imaging using an ytterbium-based laser system

DAVIDE GATTI,[1,2] MARCO LAMPERTI,[1,2] ATTILIO ZILLI,[1] FRANCESCO CANELLA,[1,2] GIULIO CERULLO,[1,2] GIANLUCA GALZERANO,[1,2] PAOLO LAPORTA,[1,2] AND NICOLA COLUCCELLI[1,2,*]

[1]*Dipartimento di Fisica - Politecnico di Milano, Piazza Leonardo da Vinci 32, 20133 Milano, Italy*
[2]*Istituto di Fotonica e Nanotecnologie - CNR, Piazza Leonardo da Vinci 32, 20133 Milano, Italy*
[*]*nicola.coluccelli@polimi.it*

Abstract: A laser system for standoff coherent anti-Stokes Raman scattering (CARS) spectroscopy of various materials under ambient light conditions is presented. The system is based on an ytterbium laser and an ultrafast optical parametric amplifier for the generation of a broadband pump tunable from 880 to 930 nm, a Stokes at 1025 nm, and a narrowband probe at 512.5 nm. High-resolution Raman spectra encompassing the fingerprint region (400-1800 cm^{-1}) are obtained in 5 ms for toluene, and 100 ms for two types of sugars, glucose and fructose, at a distance of 1 m. As a demonstration of the potential of the setup, hyperspectral images of a 2×2-cm^2 target area are collected for a toluene cuvette and a glucose/fructose pressed disk. Our approach is suitable for implementation of a portable system for standoff CARS imaging of chemical and biological materials.

1. Introduction

CARS spectroscopy has attracted a large interest for real-time detection and identification of materials at standoff distances, because of its chemical specificity, enhanced sensitivity, and high potential for fast surface scanning on virtually all surfaces [1–7]. While traditional spontaneous Raman (SR) scattering spectroscopy has been already used for a range of applications in standoff detection mode, including chemicals and minerals analysis [8,9], explosives detection [10,11], or studies of artworks [12], the small SR cross-section along with the strong interference due to fluorescence or ambient light represent severe limitations. CARS spectroscopy enhances the Raman signal by many orders of magnitude through coherent addition of molecular vibrations [13–15]. This technique has been successfully applied for gas thermometry as well as detection of explosives, and chemical/biological warfare agents at standoff or arms-length distance [1–5,7,16–18]. The main problem associated with the standoff CARS systems reported so far is instrumental: the laser source driving the system is a regeneratively amplified Ti:Sa source, which requires maintenance and can be only operated in a laboratory environment with proper temperature stabilization and vibration isolation platforms. Accordingly, there is need for a compact laser source allowing the implementation of a portable standoff CARS system to be operated onsite. The current technology of industrial ultrashort-pulse lasers provides solution to this demand, being based on platforms purposely designed for operation into harsh environments, with a high resistance against vibrations or dust, and the capability to deliver high-energy femtosecond laser pulses.

In this paper, we demonstrate a standoff CARS system based on a compact ytterbium laser suitable for identification and location of a variety of materials, including powders. The ytterbium laser drives an optical parametric amplifier (OPA) delivering pump pulses tunable in the range 880-930 nm, and provides Stokes and probe pulses by its fundamental and second harmonic at

#457373 https://doi.org/10.1364/OE.457373
Journal © 2022 Received 1 Mar 2022; revised 7 Apr 2022; accepted 7 Apr 2022; published 20 Apr 2022

Optics EXPRESS

1025 and 512.5 nm, respectively. This system allows for the observation of high-quality Raman spectra in the fingerprint region from to 400 to 1800 cm^{-1}. We present results for toluene and two types of sugars, glucose and fructose, where CARS spectra could be measured in 5 and 100 ms, respectively, at a distance of 1 m; in similar conditions, we demonstrate hyperspectral CARS imaging of a toluene cuvette and a glucose/fructose pressed disk sample.

2. Experiment and results

2.1. Yb-based ultrafast optical parametric amplifier

The layout of the OPA source used for standoff CARS experiments is shown in Fig. 1. It starts with an amplified Yb:KGW laser (Pharos, Light Conversion), generating 250-μJ, 250-fs pulses at 1025 nm and 1-kHz repetition rate, with linear horizontal polarization. A small part of the incident pulse energy, corresponding to 2.5 μJ, is used for white-light continuum (WLC) generation, while the rest of the energy is passed thought a half-wave plate and then directed onto a lithium triborate crystal (LBO, type 1, $\theta = 90°, \phi = 13.8°$, thickness 3.7 mm) for second harmonic (SH) generation at 512.5 nm. The efficiency of SH generation is 60%, yielding a SH pulse energy of 150 μJ. The orientations of the LBO crystal and half-wave plate are finely tuned in order to generate a SH with polarization mostly oriented along the vertical axis, and a small component, corresponding to 3 μJ, along the horizontal axis. The latter is used to pump the first two cascaded noncollinear OPAs ($NOPA_1$ and $NOPA_2$ in Fig. 2), while the main polarization component of the SH beam is used to pump the third OPA stage ($NOPA_3$). All OPAs are based on beta-barium borate crystals with similar characteristics (BBO, type 1, $\theta = 23.4°, \phi = 90°$) apart from the thicknesses of 1 and 2 mm for $NOPA_{1,2}$ and $NOPA_3$, respectively; moreover, they are operated in the Poynting vector compensated walk-off geometry in order to get better near-field profile of the signal beam [19]. For optimization of the performance, the phase matching angle of the BBO crystals is first set to an internal signal-pump noncollinearity angle of ~2.5°, that is the so-called "magic angle" providing the broadest spectral amplification band, and then it is finely adjusted for optimizing the gain at 910 nm.

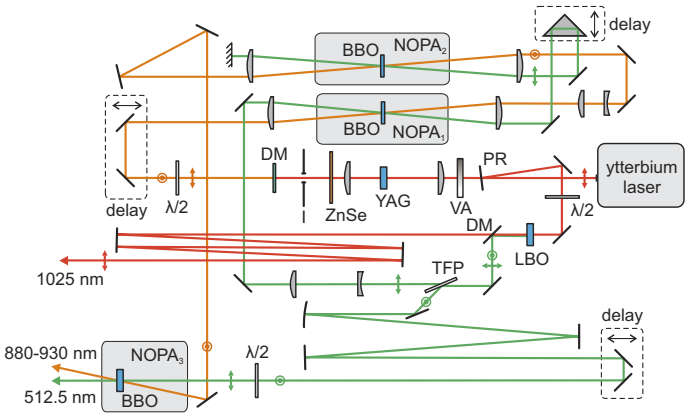

Fig. 1. Scheme of the three-stage NOPA. PR: 99% partial reflectivity mirror; DM: dichroic mirror; I: Iris; VA: variable attenuator; TFP: thin-film polarizer.

For WLC generation, laser pulses are focused by a 75-mm focal length lens to a $1/e^2$ beam diameter of 35 μm at the input face of a 6-mm-thick YAG plate. The energy of pulses is adjusted to ~1 μJ by a variable attenuator in order to generate a stable single filament within the YAG plate [20]. Additionally, the strong fundamental component at 1025 nm of the WLC pulse spectrum is rejected by a short-wave pass filter with cut-off at 980 nm. The resulting WLC spectrum, shown

Optics EXPRESS

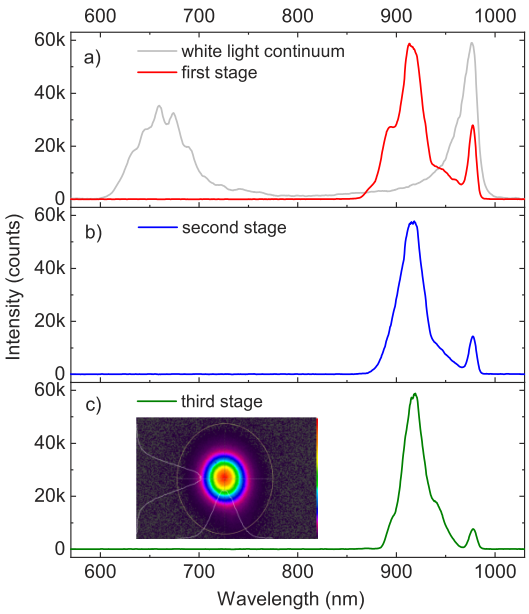

Fig. 2. Spectra of pulses at the output of each NOPA stage. The gray line represents the white-light continuum spectrum used for seeding the first NOPA stage. The inset in c) shows the far-field profile of the beam at the output of the third NOPA stage.

in Fig. 2(a), has a smooth and stable profile spanning the range from 600 to 980 nm. Before entering the OPA, the WLC pulse is temporally dispersed by a 3-mm thick zinc selenide plate in order to reduce the range of frequencies interacting with the SH pump pulse, and therefore the bandwidth of the amplified signal, to ~450 cm^{-1}. In addition, a hard aperture with diameter of 1 mm is used to improve the WLC spatial quality.

The WLC and SH beam are focused at ~10 mm before the BBO crystal of $NOPA_1$, with $1/e^2$ beam diameters of 120 and 100 μm, respectively. This design provides a soft aperture effect for the WLC beam, as parametric amplification occurs only at points where WLC and SH beams are both present, and ensures that the amplified signal at the output of the NOPA inherits the excellent spatial beam quality of the SH beam. In terms of peak intensity, the SH pump pulse energy of 3 μJ corresponds to ~180 GW/cm^2, assuming SH pulse duration of 250 fs, which is the threshold where spatial profile of the amplified signal beam starts to degrade due to nonlinear self-action processes in the BBO crystal. The energy of the amplified signal pulse at the output of $NOPA_1$ is 0.1 μJ, which corresponds to an efficiency of the parametric interaction of ~3%. According to this, $NOPA_1$ is operated well below the condition of pump depletion, and the SH pump beam can be recycled for pumping of $NOPA_2$. A similar design for the beam diameters of the seeder and SH pump has been adopted in this case, resulting in an amplified pulse energy of 0.3 μJ at the output of $NOPA_2$. The combination of $NOPA_1$ and $NOPA_2$ provides pre-amplification to an energy level suitable for effective suppression of amplified parametric fluorescence at the last parametric amplifier stage, the $NOPA_3$. Here, the beam diameter adopted for the SH pump is 1.3 mm, corresponding to a peak intensity of ~85 GW/cm^2; for the seeder, we used a slightly larger beam diameter of 1.5 mm. The energy of the amplified beam at the output of $NOPA_3$ is 21 μJ, corresponding to an overall efficiency of 8% with respect to the energy of the original Yb laser.

Figure 2 shows the spectra of signal pulses at the output of the three OPA stages, corresponding to energies of 0.1, 0.3, and 21 μJ. The pulse bandwidth is progressively reduced when passing through successive OPA stages, and the peak at 975 nm, due to parasitic amplification of the

Optics EXPRESS

strong WLC frequency components close to the fundamental, is attenuated. The final spectrum has a FWHM of 35 nm (420-cm^{-1}). The inset of Fig. 2(c) shows the high quality of the far-field spatial profile at the output of NOPA$_3$. The beam quality factors are M_x^2=1.21 and M_y^2=1.18, for the horizontal and vertical axis, respectively.

2.2. Standoff CARS setup

The layout of the setup used for standoff CARS experiments is shown in Fig. 3. The pump, Stokes, and probe pulses required for CARS interaction are derived from the Yb laser and OPA source. In detail, the pump is provided by the output pulses of the OPA, priorly compressed to minimum duration by a SF_{10} prism pair, and multiplexed to the Stokes and probe by dichroic mirrors. These last components are characterized by insertion losses of ~60%, which could be reduced by using chirped mirrors for pulse compression, and dichroic mirrors with improved performance (custom design) for multiplexing. Due to the high insertion losses, the energy of the pump pulses available on the target for standoff CARS detection is reduced to 8 μJ at 910 nm. The Stokes is the residual of the fundamental beam after SH generation, with an energy of ~90 μJ at 1025 nm, and a FWHM band of ~7 nm (70 cm^{-1}), however, it has been attenuated to ~10 μJ, before multiplexing with the pump, in order to avoid sample damage. Finally, the probe is derived from the SH pulses left unconverted after interaction in the NOPA$_3$, and spectrally narrowed in a zero dispersion pulse shaper, to reach a FWHM band of ~0.2 nm (8 cm^{-1}), with an energy of 9 μJ and a duration of ~1.5 ps. The NOPA and CARS setup are mounted on an optical breadboard with dimensions of 100×40 cm^2; commercial NOPAs with similar performance are currently available as industrial grade modules embedded into the laser case for minimum dimensions and high stability.

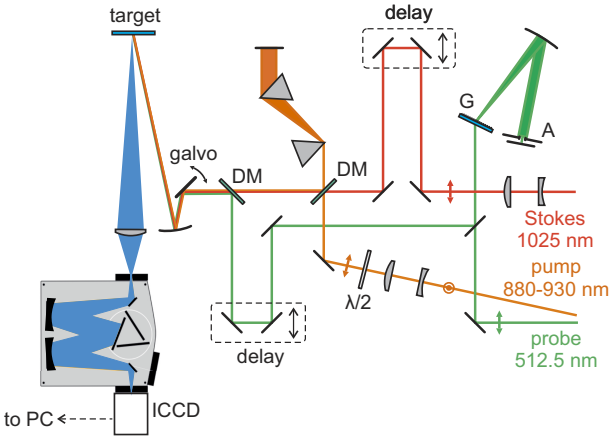

Fig. 3. Scheme of the optical system for standoff CARS detection. G: grating; A: variable slit; DM: dichroic mirror; ICCD: intensified CCD camera.

The spectra of the pump, Stokes, and probe pulses are shown in Fig. 4 along with the corresponding energies. The center wavelength of the pump pulse can be tuned from 880 to 930 nm by acting on the delay between the SH pulse and the WLC seed. This allows for tuning of the center frequency of CARS excitation from 1000 to 1600 cm^{-1}, depending on pump wavelength, with a simultaneous FWHM bandwidth of ~500-cm^{-1}, corresponding to the convoluted band of the pump and Stokes pulses, thus covering a wide portion of the fingerprint region required for molecular identification. Overall, the system provides pump, Stokes, and probe pulse energies at the level of a few microjoules, as required for effective excitation of CARS signal in standoff configurations. Two separate delay lines are used to synchronize the three pulses for CARS

Optics EXPRESS

interaction. The beams are multiplexed in a collinear arrangement and then focused by a spherical mirror onto the target sample, placed at the standoff distance of 1 m. The $1/e^2$ diameter of the three laser beams onto the target is 360 μm. The back-scattered CARS signal is collected by a 2-inches lens with 150-mm focal length and focused onto the entrance slit of a spectrometer equipped with an intensified CCD camera (gating time of 2 ns).

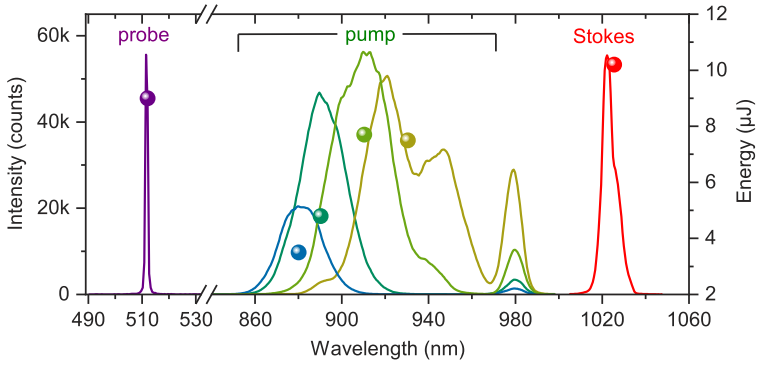

Fig. 4. Spectra of the pump (tunable), Stokes, and probe pulses incident onto the target. The corresponding pulse energies are shown with circles.

The compressed laser pulses generated by the OPA have been characterized in the time and frequency domain by SH frequency resolved optical gating (SH-FROG) analysis. Figures 5(a) and 5(b) show the experimental and retrieved SH-FROG maps for the pulses centered at 910 nm, while Figs. 5(c) and (d) show the retrieved temporal and spectral intensity and phase profiles (rms retrieval error 0.68%), along with the experimental spectrum. The spectral phase in Fig. 5(c) shows a residual negative quadratic phase (negative chirp) ascribed to sub-optimal compensation of pulse dispersion by the SF_{10} prism compressor, however, the measured pulsewidth of 43 fs is very close to the transform limited value (39 fs), meaning that overall the spectral phase is well compensated, and the residual chirp has only a marginal effect on pulse duration.

The long term stability of pulses at the output of the OPA source has been characterized by acquiring a sequence of spectra and corresponding energies at time steps of 100 ms. The laser system is placed in a laboratory without active temperature stabilization and mounted on an optical table. The data are shown in Fig. 6. The resulting power and wavelength fluctuations [21] of pulses, at an energy of 21 μJ and a center wavelength of 910 nm, are equal to ±0.9% rms and ±0.18 nm rms, respectively, over a time window of 150 minutes.

2.3. Standoff CARS spectroscopy and imaging

The general theory underlying CARS spectroscopy has been extensively studied elsewhere [22,23]. Here, we use a variant of time-resolved CARS called hybrid-CARS, that allows for observing the vibrational evolution following electronic excitation while maintaining both time and frequency resolution [18,24,25]. Briefly, the broadband synchronized ultrashort pump and Stokes pulses at frequencies ω_p and ω_S, respectively, interact with virtual levels to create a vibrational coherence in an ensemble of molecules, simultaneously exciting a number of vibrations at frequency $\Omega_i = \omega_p - \omega_S$. This coherence is then read by the narrowband probe pulse, at frequency ω_{pr}, which generates the spectrum at the anti-Stokes frequencies $\omega_{aS} = \omega_{pr} + \Omega_i$. The probe pulse comes at a delay τ comparable with the decay time of the vibrational coherence, and the intensity of the CARS signal at Ω_i decays exponentially, with the time constant being the vibrational dephasing time of the mode at Ω_i. The CARS signal is superimposed on the so-called non-resonant background (NRB), which is due to a four-wave mixing process between pump,

Optics EXPRESS

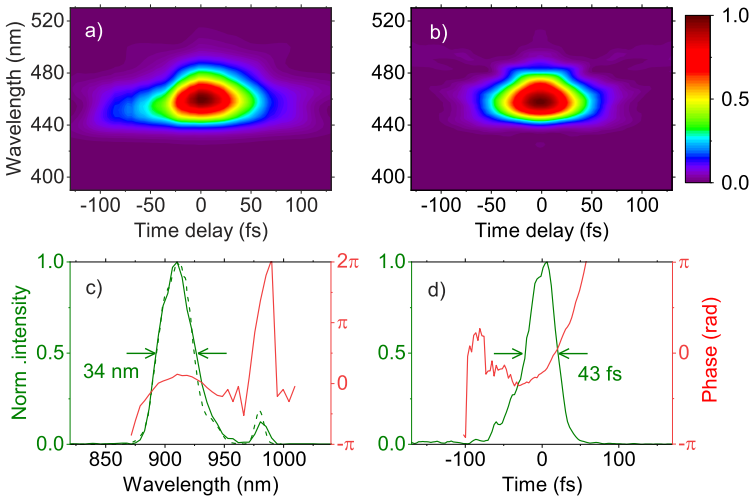

Fig. 5. Characterization of laser pulses at the output of the third NOPA stage tuned at 910 nm for highest energy. a) Measured SHG-FROG trace, and b) reconstructed FROG trace with 0.007 error on a 512 × 512 grid. c) Reconstructed (solid) and measured (dotted) spectral intensity and phase. d) Reconstructed temporal intensity and phase.

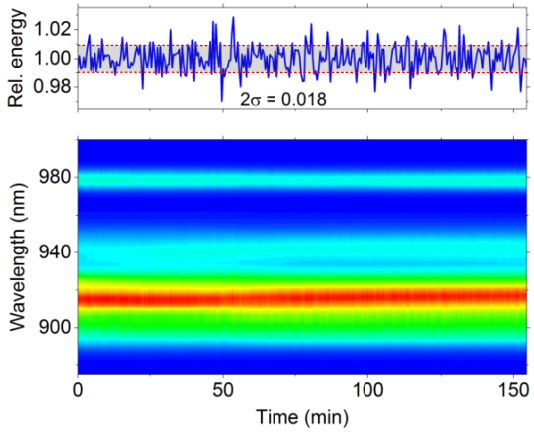

Fig. 6. Long-term power stability of the three-stage NOPA: fluctuations of pulse energy (normalized) and temporal drifting of output spectra are shown on top and bottom, respectively.

Optics EXPRESS

Stokes and probe pulses, mediated by the non-resonant third-order nonlinearity of the molecules under study and of the surrounding medium, generating light at frequency $\omega_{NRB} = \omega_{pu} - \omega_S + \omega_{pr}$. Therefore, the NRB is a broad and featureless spectrum which overlaps with the CARS peaks and can even distort their lineshapes. As the NRB relies only on non-resonant interactions with virtual states, it requires temporal overlap among the pump, Stokes and probe pulses and can be effectively reduced by delaying the probe with respect to the pump/Stokes.

Figure 7 shows the results of standoff CARS spectroscopy obtained with samples of toluene, glucose and fructose powders, at a distance of 1 m from the laser system, with the pump pulse tuned at 930 nm. In particular, Fig. 7(a), (b) and (c), show the spectrograms, obtained by plotting the CARS spectra as a function of the probe delay τ, whereas Fig. 7(d), (e) and (f) show the cross-sections of spectrograms obtained at probe delays of 3 ps for toluene, and 0.9 ps for glucose and fructose, along with the reference spectra based on SR.

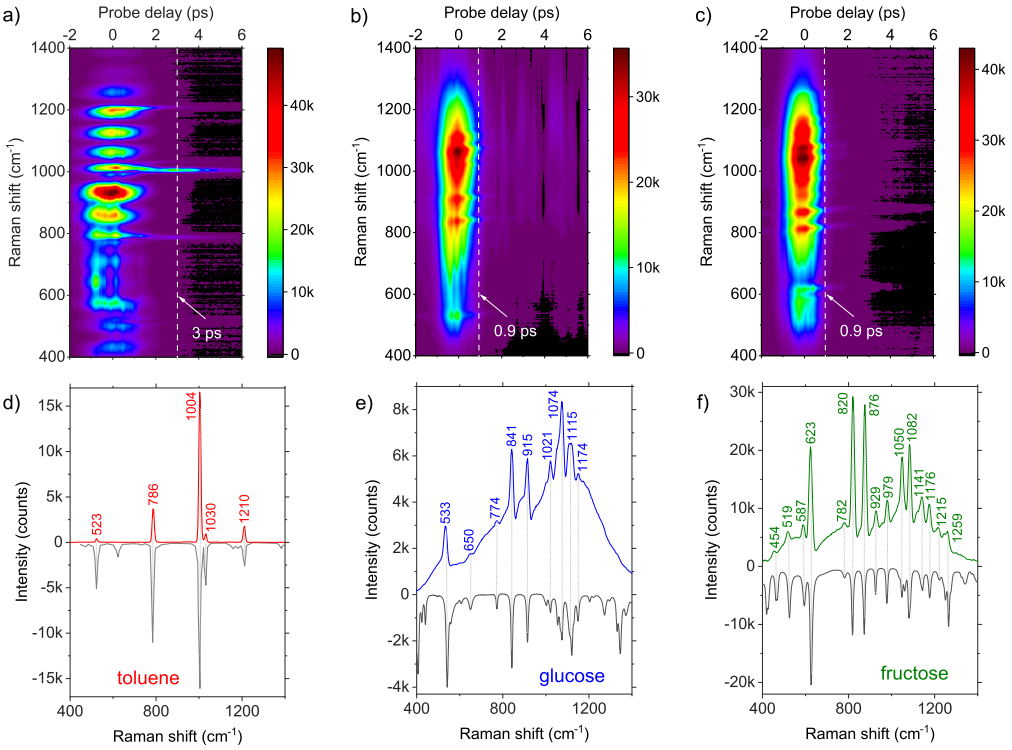

Fig. 7. CARS spectrogram of a) toluene, b) glucose, and c) fructose, as measured at standoff distance of 1 m. The cross-sections (spectra) indicated by white dotted lines are shown in d), e), and f) for toluene, glucose, and fructose, respectively. Grey lines represents the reference spectra as measured with SR microspectrometer (excitation laser wavelength of 1064 nm). For toluene, all pulse energies of pump, Stokes and probe have been set to ~0.5 μJ, and CCD integration time is 5 ms; for glucose and fructose, pulse energies of pump, Stokes and probe have been set to 7, 8, and 7 μJ, respectively, and CCD integration time is 100 ms.

Toluene is a golden standard in Raman spectroscopy featuring intense and sharp peaks, which has been used here to test the performance of our system in terms of spectral resolution and spectral coverage, and to calibrate the frequency axis of the spectrometer for hyperspectral imaging. The sample is placed within a quartz cuvette with internal path length of 1 mm. The standoff CARS spectra have been measured with an integration time of 5 ms and pulse energies of ~0.5 μJ for pump, Stokes, and probe. The streaklike horizontal lines apparent in Fig. 7(a)

Optics EXPRESS

are the signature of excited Raman transitions of toluene, while the broadband pedestal visible at zero delay is the NRB. To reduce further the NRB, a polarization based detection scheme [26] has been implemented by placing a polarizer at the spectrometer input to reject the main component of NRB with polarization perpendicular to the probe. Note that the spectrogram is characterized by strong modulations due to interference of spectral components (both resonant and nonresonant) originated from the combined action of the pump and Stokes pulse with those from the broadband pump pulse alone (the high/low frequency tails of the spectrum act as the pump/Stokes). At a probe delay of 3 ps, the NRB is largely attenuated, due to the negligible temporal overlap between pump/Stokes and probe. Under these conditions, almost all of the characteristic Raman peaks of toluene in the fingerprint region are visible. The standoff CARS spectrum shows a remarkably good agreement with the reference SR spectrum. The frequency axis has been calibrated to the Raman peaks at 786, 1004, and 1210 cm^{-1} (three-points linear fit); after this, the accuracy on the determination of vibrational frequencies is of ± 1 cm^{-1} as compared to data from SR spectrometer [27], confirming that distortions and frequency-shifting effects of CARS features due to interference with the NRB are negligible at probe delays of 3 ps. The resolution of CARS spectra is 8 cm^{-1}, as resulting from the FWHM of the peak at 1004 cm^{-1}. This is also confirmed by the doublet at 1004/1030 cm^{-1}, which is fully resolved apart from the significant attenuation of intensity at 1032 cm^{-1} due to proximity to a minimum of the interference pattern, as seen by the modulations in the NRB. The potential impact of the residual chirp of the pump pulse on the spectral excitation efficiency has been investigated by observing the frequency shift of the NRB induced by changing the delay between the pump and Stokes pulses for different amounts of material dispersion (pulse chirp) by the SF_{10} prism compressor [28]; it has been found that, in optimized conditions of minimum pump pulse duration, the effect of the residual chirp is negligible.

Glucose and fructose in the form of powder represent more challenging samples to test the performance of the standoff CARS setup. The problem in this case is related to the diffusive nature of the target which reduces dramatically the collection efficiency of the system; in particular, taking into account the 2-inch diameter and 1-m distance of the collecting lens, a rough estimation of the collection efficiency is 10^{-3}. In addition, glucose and fructose have typical Raman cross-sections and linewidths of $\sim 5.6 \times 10^{-30}$ cm^2 $molecule^{-1}$ sr^{-1} and ~ 7 cm^{-1} [29,30], respectively, to be compared with 1.38×10^{-29} cm^2 $molecule^{-1}$ sr^{-1} and ~ 2 cm^{-1} for toluene [31,32], as reported for an excitation laser wavelength of 514.5 nm, for both cases. This corresponds to a ratio between cross-sections and linewidths of glucose/fructose and toluene of ~0.4 and ~3.5, respectively. As the power of generated CARS signal is proportional to the square of the ratio between the cross-section and the linewidth for a given substance [33], the power of CARS signal from glucose/fructose is expected to be a factor $(0.4/3.5)^2 \simeq 1.3 \times 10^{-2}$ lower with respect to toluene. On the other side, it should be also considered that, in the case of toluene, the CARS signal collected by the spectrometer is due to Fresnel reflection at the quartz/air cuvette interface, which corresponds to ~4% of total CARS power. Overall, the power of the CARS signal collected by the spectrometer with glucose/fructose is expected to be a factor $0.001 \times 0.013/0.04 \simeq 3 \times 10^{-4}$ lower than toluene in similar conditions, that is three to four orders of magnitude lower. To compensate for the large signal attenuation, the energy of the pump, Stokes and probe pulses have been increased to 7, 8, and 7 μJ, respectively, while the the integration time of the intensified CCD camera has been set to 100 ms. Due to the weak Raman transitions of glucose and fructose, and to the faster vibrational dephasing times which follows from broader linewidths, it is no longer possible to isolate the resonant CARS signature with respect to the NRB by using sufficiently large probe delays, as this would just turn the SNR and overall quality to low levels. Moreover, it should be noted that the polarization based detection scheme used with toluene is uneffective here for attenuation of the NRB, because of multiple scattering inside powders which does not preserve polarizations. The best compromise

Optics EXPRESS

in terms of probe delay for optimization of the signal-to-NRB ratio is experimentally found to be ~0.9 ps. In this case, all relevant Raman lines of glucose and fructose are visible and fairly resolved while distortions due to interference with the NRB are kept sufficiently low. Peak frequencies are found to be within ±3 cm^{-1} with respect to reference spectra [30], providing satisfactory accuracy for applications requiring identification of the Raman signature, such as the hyperspectral imaging shown below. Interestingly, a horizontal cross-section of the spectrogram provides a measurement of the convolution between the pump/Stokes and probe pulses, with a FWHM duration of 1.8 ps; taking into account the durations of pump and Stokes pulses (43 and 250 fs, respectively), the resulting duration of the probe pulse is ~1.5 ps, corresponding to a FWHM band of 0.25 nm (9.5 cm^{-1}), assuming Gaussian profile of the probe spectrum, in compliance with the resolution observed in the CARS spectra. The spectrograms in Fig. 7 do not show the nodes typical of sinc-shaped probe pulses, as in previous hybrid-CARS setup featuring slit-based pulse shaper; this is ascribed to the competing diffraction effects in our pulse shaper which reduces the visibility of nodes at small slit apertures (small FWHM band of probe pulses); under this condition, the probe spectrum resembles a Gaussian rather than a rectangular profile.

It is worth to note that the large mismatch between the durations of pump and Stokes pulses adopted here, specifically 43 and 250 fs, respectively, introduces a time gating effect into the excited Raman coherence, ultimately leading to reduced efficiency of the excitation process. The configuration could be improved by using the broadband idler pulses generated within the OPA source as the Stokes, however, in this case system complexity will be increased due to the need for additional pulse compression optics; the spatial chirp of idler pulses is another potential issue to be investigated [34].

The results of hyperspectral imaging are shown in Figs. 8 and 9, for a 1-mm thick quartz cuvette filled with neat toluene and a pressed disk of glucose/fructose. In both cases, the target is placed at 1 m from the system, and the dimensions of the imaged area are 2×2 cm^2, with spatial sampling of 40×40 = 1600 pixels, corresponding to pixel size of 500×500 μm^2. As the beam diameter onto the target is 360 μm, this ensures that spectral information comes from separate points on the image. A galvo mirror deflector has been used for scanning the beam across the target. At each point (pixel), a CARS spectrum is acquired by the intensified CCD camera of the spectrometer and sent to the pc memory, where it is stored till the end of the acquisition; subsequently, a built-in Matlab *Classification Learner* application has been used for identification of substances and for constructing hyperspectral images. The classifier is based on a machine learning algorithm, which provides with all the flexibility required for recognizing similarities among highly variable spectra, as for the imaging of powders (glucose/fructose) demonstrated here, where the inherent variance of sample properties and dimensions affects the quality and reproducibility of the spectra. According to the general working principle of machine learning classifiers, the machine has been first trained using a set of reference SR spectra of many different solvents and materials, including toluene, glucose, and fructose. Once the classifier is ready, the acquired 40×40 spectra of a single hyperspectral image (matrix) are used as input data.

An important point is related to the calibration of the frequency axis. In particular, as the beam is scanned across a horizontal line on the sample, the dispersed image (spectrum) acquired by the spectrometer translates horizontally across the CCD camera sensor, which corresponds to a translation along the frequency axis. The frequency shift is strictly proportional (i.e. non-linearities are negligible) to the horizontal displacement of the imaged point with respect to the center, as verified experimentally. Once the proportionality factor between the frequency shift and horizontal displacement has been calculated, it is possible to apply a suitable correction (frequency shift) to the observed spectra prior to processing by the classifier.

For hyperspectral imaging of the toluene cuvette shown in Fig. 8, the pixel dwell time has been set to 5 ms, which allows for a complete scan of the target area within 13 s, including data processing. The reconstructed image is of high quality, as it can be seen from the accurate

Optics EXPRESS

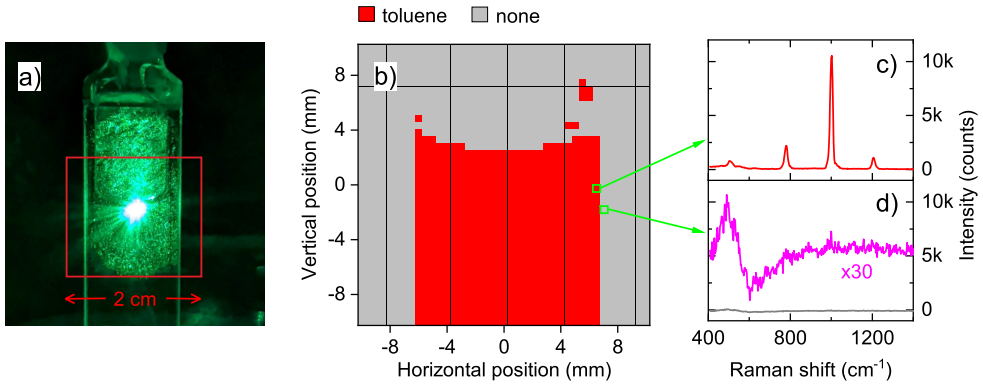

Fig. 8. Standoff CARS imaging of a cuvette filled with toluene at a distance of 1 m from the laser source. a) Photograph showing the area scanned by the laser beam; b) reconstructed image based on output of the classifier; c,d) CARS spectra for two pixels corresponding to toluene (red line) and quartz (gray line); the pink line is a replica of the gray line enlarged by a factor of 30. The concave meniscus occurring in the upper surface of toluene can be appreciated in the CARS image. Pump, Stokes, probe pulse energy, ~0.5 μJ; probe delay, 3 ps; number of pixels, 40 × 40; pixel dwell time 5 ms; measurement time (including data processing), 13 s.

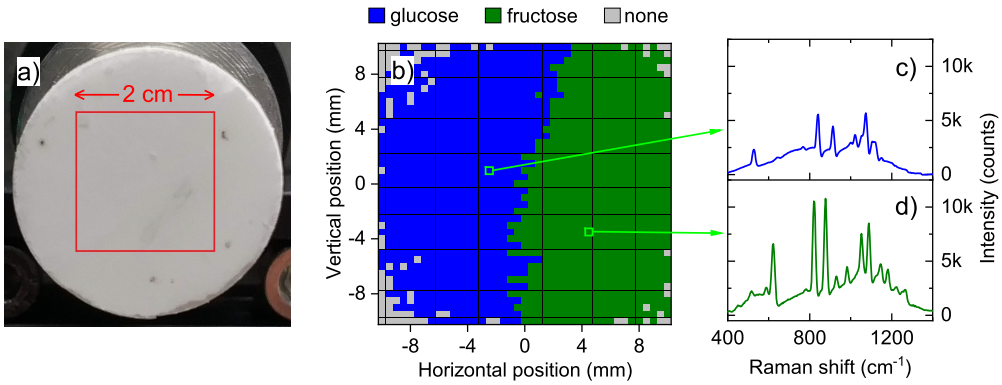

Fig. 9. Standoff CARS imaging of a tablet made of glucose and fructose at a distance of 1 m from the laser source. a) Photograph showing the area scanned by the laser beam; b) reconstructed image based on output of the classifier; c,d) CARS spectra for two pixels corresponding to glucose (blue line) and fructose (green line). Glucose and fructose are indistinguishable by eye, however they can be readily mapped by CARS imaging. Pump pulse energy, 7 μJ; Stokes pulse energy, 8 μJ; probe pulse energy, 7 μJ; probe delay, 0.9 ps; number of pixels, 40 × 40; pixel dwell time 50 ms; measurement time (including data processing), 1 min 25 s.

Optics EXPRESS

reconstruction at the toluene/glass and toluene/air interfaces, especially the meniscus and the small droplets formed by toluene on the walls of the cuvette. In the case of the pressed disk of glucose/fructose, the situation becomes more challenging because of the reduced backscattering CARS signal collected by the spectrometer, especially on the borders of the imaged area, where additional losses due to vignetting inside the spectrometer bring the SNR to a level which prevents confident identification. Quantitatively, the precision of the classifier for identification of glucose and fructose has been tested using neat samples. The identification software has been set to discard the spectra where the main peak has a signal-to-noise ratio lower than 10. According to this assumption, a few pixels close to the corners of the reconstructed image in Fig. 9 are unclassified. Under these conditions, the precision of the classifier is found to be 96% (TP/TP+FP, TP=True Positive, FP=False Positive), attesting the high confidence of a positive identification. The hyperspectral image allows to discriminate readily between glucose and fructose, while the two types of sugars are totally undistinguishable by eye, as apparent from the photograph reported in Fig. 9.

3. Conclusion

We have demonstrated standoff CARS spectroscopy and imaging using a laser system based on a diode-pumped ytterbium laser and an OPA source. We used the so-called hybrid-CARS technique, which was implemented previously only by large Ti:Sapphire laser systems, unsuited for operation outside of a laboratory environment. Being based on a compact ytterbium laser, our system provides a portable platform which can be readily utilized for applications on-field. We demonstrated the capability of the system to identify different materials, such as solvents and powders, at a standoff distance of 1 m as well as to perform high-resolution hyperspectral imaging of solvents and powders. Due to its on-field deployability, we expect our system to find application in homeland security for the detection of explosives or bio-chemical weapons, as well as studies and preservation of artworks, and planet exploration.

Disclosures. The authors declare no conflicts of interest.

Data availability. Data underlying the results presented in this paper are not publicly available at this time but may be obtained from the authors upon reasonable request.

References

1. M. T. Bremer, P. J. Wrzesinski, N. Butcher, V. V. Lozovoy, and M. Dantus, "Highly selective standoff detection and imaging of trace chemicals in a complex background using single-beam coherent anti-stokes raman scattering," Appl. Phys. Lett. **99**(10), 101109 (2011).
2. M. T. Bremer and M. Dantus, "Standoff explosives trace detection and imaging by selective stimulated raman scattering," Appl. Phys. Lett. **103**(6), 061119 (2013).
3. H. Li, D. A. Harris, B. Xu, P. J. Wrzesinski, V. V. Lozovoy, and M. Dantus, "Standoff and arms-length detection of chemicals with single-beam coherent anti-stokes raman scattering," Appl. Opt. **48**(4), B17–B22 (2009).
4. G. Rasskazov, A. Ryabtsev, and M. Dantus, "Eye-safe near-infrared trace explosives detection and imaging," Opt. Express **25**(6), 5832–5840 (2017).
5. O. Katz, A. Natan, Y. Silberberg, and S. Rosenwaks, "Standoff detection of trace amounts of solids by nonlinear raman spectroscopy using shaped femtosecond pulses," Appl. Phys. Lett. **92**(17), 171116 (2008).
6. M. O. Scully, G. W. Kattawar, R. P. Lucht, T. Opatrný, H. Pilloff, A. Rebane, A. V. Sokolov, and M. S. Zubairy, "Fast cars: Engineering a laser spectroscopic technique for rapid identification of bacterial spores," Proc. Natl. Acad. Sci. **99**(17), 10994–11001 (2002).
7. D. Pestov, X. Wang, G. O. Ariunbold, R. K. Murawski, V. A. Sautenkov, A. Dogariu, A. V. Sokolov, and M. O. Scully, "Single-shot detection of bacterial endospores via coherent raman spectroscopy," Proc. Natl. Acad. Sci. **105**(2), 422–427 (2008).
8. A. K. Misra, S. K. Sharma, C. H. Chio, P. G. Lucey, and B. Lienert, "Pulsed remote raman system for daytime measurements of mineral spectra," Spectrochimica Acta Part A: Mol. Biomol. Spectrosc. **61**(10), 2281–2287 (2005).
9. S. K. Sharma, P. G. Lucey, M. Ghosh, H. W. Hubble, and K. A. Horton, "Stand-off raman spectroscopic detection of minerals on planetary surfaces," Spectrochim Acta A Mol Biomol Spectrosc **59**(10), 2391–2407 (2003).
10. J. C. Carter, S. M. Angel, M. Lawrence-Snyder, J. Scaffidi, R. E. Whipple, and J. G. Reynolds, "Standoff detection of high explosive materials at 50 meters in ambient light conditions using a small raman instrument," Appl. Spectrosc. **59**(6), 769–775 (2005).

Optics EXPRESS

11. A. Pettersson, S. Wallin, H. Astmark, A. Ehlerding, I. Johansson, M. Nordberg, H. Ellis, and A. Al-Khalili, "Explosives standoff detection using Raman spectroscopy: from bulk towards trace detection," in *Detection and Sensing of Mines, Explosive Objects, and Obscured Targets XV*, vol. 7664 R. S. Harmon, J. H. H. Jr., and J. T. Broach, eds., International Society for Optics and Photonics (SPIE, 2010), pp. 472–483.
12. P. Vandenabeele, K. Castro, M. Hargreaves, L. Moens, J. Madariaga, and H. Edwards, "Comparative study of mobile raman instrumentation for art analysis," Anal. Chim. Acta **588**(1), 108–116 (2007).
13. C. L. Evans, E. O. Potma, and X. S. Xie, "Coherent anti-stokes raman scattering spectral interferometry: determination of the real and imaginary components of nonlinear susceptibility χ^3 for vibrational microscopy," Opt. Lett. **29**(24), 2923–2925 (2004).
14. E. O. Potma, C. L. Evans, and X. S. Xie, "Heterodyne coherent anti-stokes raman scattering (CARS) imaging," Opt. Lett. **31**(2), 241–243 (2006).
15. D. Pestov, G. O. Ariunbold, X. Wang, R. K. Murawski, V. A. Sautenkov, A. V. Sokolov, and M. O. Scully, "Coherent versus incoherent raman scattering: molecular coherence excitation and measurement," Opt. Lett. **32**(12), 1725–1727 (2007).
16. R. Santagata, M. Scherman, M. Toubeix, M. Nafa, B. Tretout, and A. Bresson, "Ultrafast background-free ro-vibrational fs/ps-cars thermometry using an yb:yag crystal-fiber amplified probe," Opt. Express **27**(23), 32924–32937 (2019).
17. E. Vicentini, A. Gambetta, G. Galzerano, P. Laporta, K. Curtis, K. McEwan, C. R. Howle, and N. Coluccelli, "Fiber laser system for standoff coherent raman spectroscopy," Opt. Lett. **45**(21), 5925–5928 (2020).
18. D. Pestov, R. K. Murawski, G. O. Ariunbold, X. Wang, M. Zhi, A. V. Sokolov, V. A. Sautenkov, Y. V. Rostovtsev, A. Dogariu, Y. Huang, and M. O. Scully, "Optimizing the laser-pulse configuration for coherent raman spectroscopy," Science **316**(5822), 265–268 (2007).
19. T. Stanislauskas, I. Balčiūnas, V. Tamuliene, R. Budriūnas, and A. Varanavičius, "Analysis of parametric fluorescence amplified in a noncollinear optical parametric amplifier pumped by the second harmonic of a femtosecond yb:kgw laser," Lith. J. Phys. **56**(1), 1–8 (2016).
20. A. Dubietis, G. Tamosauskas, R. Åuminas, V. Jukna, and A. Couairon, "Ultrafast supercontinuum generation in bulk condensed media (invited review)," Lith. J. Phys. **57**(3), 113 (2017).
21. The rms wavelength fluctuation is calculated as follows: first, the mean wavelength $\bar{\lambda}_i$ of the spectrum $S(\lambda)_i$ is calculated for i=1, . . . , M, with M being the number of spectra acquired over the observation time window. Then, the rms wavelength fluctuation is obtained as the standard deviation of $\bar{\lambda}_i$.
22. G. P. Agrawal, "Chapter 10 - four-wave mixing," in *Nonlinear Fiber Optics (Fourth Edition)*, G. P. Agrawal, ed. (Academic Press, San Diego, 2006), Optics and Photonics, pp. 368–423, fourth edition ed.
23. T. W. Kee, H. Zhao, and M. T. Cicerone, "One-laser interferometric broadband coherent anti-stokes raman scattering," Opt. Express **14**(8), 3631–3640 (2006).
24. B. D. Prince, A. Chakraborty, B. M. Prince, and H. U. Stauffer, "Development of simultaneous frequency- and time-resolved coherent anti-stokes raman scattering for ultrafast detection of molecular raman spectra," J. Chem. Phys. **125**(4), 044502 (2006).
25. H. U. Stauffer, J. D. Miller, S. Roy, J. R. Gord, and T. R. Meyer, "Communication: Hybrid femtosecond/picosecond rotational coherent anti-stokes raman scattering thermometry using a narrowband time-asymmetric probe pulse," J. Chem. Phys. **136**(11), 111101 (2012).
26. D. Oron, N. Dudovich, and Y. Silberberg, "Femtosecond phase-and-polarization control for background-free coherent anti-stokes raman spectroscopy," Phys. Rev. Lett. **90**(21), 213902 (2003).
27. Chemical Book, https://www.chemicalbook.com/SpectrumEN_108-88-3_Raman.htm.
28. D. Pestov, X. Wang, R. K. Murawski, G. O. Ariunbold, V. A. Sautenkov, and A. V. Sokolov, "Pulse shaping for mode-selective ultrafast coherent raman spectroscopy of highly scattering solids," J. Opt. Soc. Am. B **25**(5), 768–772 (2008).
29. R. L. McCreery, *Raman Spectroscopy for Chemical Analysis*, Chemical analysis 157 (John Wiley & Sons, 2000).
30. S. Söderholm, Y. H. Roos, N. Meinander, and M. Hotokka, "Raman spectra of fructose and glucose in the amorphous and crystalline states," J. Raman Spectrosc. **30**(11), 1009–1018 (1999).
31. Y. Kato and H. Takuma, "Experimental study on the wavelength dependence of the raman scattering cross sections," J. Chem. Phys. **54**(12), 5398–5402 (1971).
32. W. R. L. Clements and B. P. Stoicheff, "Raman linewidths for stimulated threshold and gain calculations," Appl. Phys. Lett. **12**(8), 246–248 (1968).
33. W. M. Tolles, J. W. Nibler, J. R. McDonald, and A. B. Harvey, "A review of the theory and application of coherent anti-stokes raman spectroscopy (CARS)," Appl. Spectrosc. **31**(4), 253–271 (1977).
34. C. Manzoni and G. Cerullo, "Design criteria for ultrafast optical parametric amplifiers," J. Opt. **18**(10), 103501 (2016).